

An acoustic technique for measurement of bubble solids mass loading – (a) Fundamental study of single bubble

Wen Zhang^{*}, Steven J. Spencer, Peter Coghil

Lucas Heights Research Laboratory, CSIRO Process Science and Engineering, Locked Bag 2005, Kirrawee, New South Wales 2232, Australia

ARTICLE INFO

Article history:

Available online 6 March 2012

Keywords:

Flotation bubbles
On-line analysis
Process instrumentation

ABSTRACT

This paper investigates a promising acoustic emission (AE) technique for estimating solids mass loading on pulp bubbles, with potential for on-line monitoring of attached solids in industrial flotation cells. It is observed that the coating of solids on a bubble surface results in a decrease in the fundamental (Minnaert) AE resonance frequency. Analytical models are derived to relate the resonance frequency of a loaded bubble to its size, attached solids mass loading and geometrical covering of particles. The AE resulting from induced pulsations of a solids loaded bubble is measured and linked with high-speed photographic recordings of the oscillations. These experiments have been performed for the attachment of a monolayer, multilayer and cluster of particles onto a gas bubble. The efficacy of the monitoring approach for these types of solids loading is demonstrated and a comparison is made of the sophistication of modelling necessary for adequate prediction of attached solids mass loading.

© 2012 Elsevier Ltd. All rights reserved.

1. Introduction

Bubble solids loading (attachment) is one of the key processes related to flotation performance (Bradshaw and O'Connor, 1996; Ross, 1997). On-line measurement of solids mass loading on bubbles in industry flotation cells is clearly highly desirable for process optimisation purposes. One approach reported in the literature is a device using the positive displacement principle to collect solids laden bubbles at different depths in the pulp phase of a flotation machine and accumulate them into a reservoir, allowing the solids load to be weighed (Dyer, 1995; Moys et al., 2010; Seaman et al., 2004). Reproducible bubble load measurements have been reported using this technique. However, the limitations of this instrument include a large sample mass (i.e., at least 200 g of solids (Bhondayi, 2010)) required for accurate estimation of solids loading and loss of attached fine particles with the displaced water during bubble bursting in the reservoir.

Video image analysis and direct sampling of the froth surface have also been combined to measure the bubble solids loading in the froth phase (Barbian et al., 2007; Sadr-Kazemi and Cilliers, 2000; Ventura-Medina et al., 2004). This technique uses a microscope glass to sample the curved surface of a single bubble, with calculation of the bubble solids loading as the amount of solids on the slide over the surface area of the bubble. Under steady state conditions, this technique requires that the upper surface of the froth be video recorded for off-line image processing.

In this paper, an acoustic emission technique is investigated for measurement of pulp bubble solids mass loading. The strong acoustic resonance and scattering properties associated with a bubble immersed in a liquid make acoustic techniques potentially useful for estimation of pulp bubble properties and dynamics. The acoustic resonance frequency for a freely oscillating bubble may be defined as (Minnaert, 1993)

$$f_0 = \frac{1}{2\pi R_0} \sqrt{\frac{3\kappa P_0}{\rho_l}} \quad (1)$$

Here f_0 is the fundamental resonance frequency, R_0 is the bubble equilibrium radius, κ is the polytropic index, P_0 is the absolute liquid pressure, and ρ_l is the liquid density. Thus, the bubble equilibrium radius can be estimated from knowledge of the acoustic resonance frequency.

Solids attachment on a bubble surface alters bubble dynamics. As intuitively expected, the added mass causes a decrease in the acoustic resonance frequency associated with the original unloaded bubble. In this paper, theoretical formulae are derived to relate bubble attached mass loading and distribution to acoustic resonance frequency. The resonance frequency of the attached solids loaded bubble is found to be a function of the unloaded bubble resonance frequency, the bubble equilibrium radius, the solids mass loading, the thickness of the attached solid–liquid agglomerate layer and the solids coverage angle. The resonance of a particle-laden bubble is measured to validate the model, where active acoustic techniques are applied to force the bubble into linear oscillation. A variety of solids attachment geometries on the gas

^{*} Corresponding author. Tel.: +61 2 9710 6744; fax: +61 2 9710 6789.

E-mail address: W.Zhang@csiro.au (W. Zhang).

bubble, i.e., a monolayer, a multilayer and a cluster of particles, are investigated. The sophistication of modelling necessary for adequate prediction of attached solids mass loading is discussed. It is noted that in flotation there typically are large numbers of bubbles in close proximity, so group acoustic effects may be significant. However, the investigation of the acoustic response of a single bubble with solids loading, as made in this study, is a necessary foundation for subsequent group studies, and remains relevant to flotation monitoring based on engineering an active monitoring system that insonates and monitors a small number of bubbles at any sampling point.

2. Theory

2.1. Model development

We begin by building on the model for spherical bubble unforced oscillations in a liquid as described in Leighton (1994). A solids loaded bubble freely-oscillating or subject to a low power driving sound field at resonance frequency undergoes simple harmonic oscillation, with the translation of the bubble wall about the mean radius R_0 described by $R_t = R_0 e^{i\omega_p t}$, where R_0 is the amplitude of oscillation and $\omega_p = 2\pi f_p$ is the resonance frequency. The loaded bubble radius is therefore

$$R = R_0 + R_0 e^{i\omega_p t}. \quad (2)$$

The aim here is to find the mathematical relation between f_p and f_0 associated with the original unloaded bubble, based on physical parameters such as bubble size, solids mass loading, and particle coverage geometry.

During the oscillation, the bubble kinetic energy is assumed to be dominated by that associated with a layer of solid-liquid agglomerate (representing slurry composed of attached particles and interstitial liquid) plus the moving liquid external to the bubble and surrounding layer. As shown in Fig. 1, the solids geometrical coverage on the bubble surface is represented by the coverage angle θ_c , which is defined as the angle formed by the edge of the coverage on the bubble surface, the centre of the spherical bubble, and the lowest point of the bubble, in the vertical plane with gravity pointing downwards. The assumption here is that solids cover-

age on the bubble surface has uniform thickness and is symmetric with respect to an axis defined by the direction of gravity. A further assumption of these models is that in terms of acoustic measurement, the most significant component of the bubble oscillations is still the spherically symmetric 'breathing' mode, despite the coverage angle introducing an angular dependence into the attached mass loading (the higher modes are by theory much weaker acoustic emitters (Leighton, 1994)). The kinetic energy associated with the attached solid-liquid agglomerate is:

$$\varphi_s = \frac{1}{2} M_{sl} \dot{R}^2, \quad (3)$$

where $M_{sl} = \frac{M_s \rho_{sl}}{\delta_s \rho_s}$ is the total mass of the attached solid-liquid agglomerate, M_s is the mass of attached solids on the bubble, and ρ_s and ρ_{sl} are the density of solids and solid-liquid agglomerate, respectively. Here δ_s is the volumetric fraction of particles in the attached solid-liquid agglomerate. The thickness of the attached solid-liquid agglomerate layer can therefore be represented as

$$\varepsilon = \frac{M_s}{2\pi R_0^2 (1 - \cos \theta_c) \rho_s \delta_s}. \quad (4)$$

The kinetic energy of the liquid outside the bubble (and attached solid-liquid agglomerate layer) is found by integrating over shells of liquid from the bubble wall to infinity. Based on the solids coverage geometry (the coverage angle θ_c), the region of integration from the bubble wall is divided into two parts, one being the region from the bubble wall where solids are attached (integration from $R + \varepsilon$ to infinity) and the other being from the bubble wall where no solids are attached (integration from R to infinity). A shell line element at radius r and angle θ has thickness dr and mass $2\pi r^2 \rho_l dr \sin \theta d\theta$. Therefore, the total kinetic energy of the moving liquid surrounding the bubble is defined by

$$\varphi_l = \frac{1}{2} \left[\int_0^{\theta_c} \int_{R+\varepsilon}^{\infty} 2\pi r^2 \dot{r}^2 \rho_l dr \sin \theta d\theta + \int_{\theta_c}^{\pi} \int_R^{\infty} 2\pi r^2 \dot{r}^2 \rho_l dr \sin \theta d\theta \right]. \quad (5)$$

The total kinetic energy associated with the attached solid-liquid agglomerate and the surrounding liquid (ignoring the relatively small contribution from the gas in the bubble) is

$$\varphi_k = \varphi_s + \varphi_l. \quad (6)$$

Based on the assumption that both the liquid and solid-liquid agglomerate are incompressible, equating the mass of liquid flow across any surface outside the bubble to the flow at the bubble wall gives $\dot{r}/R = R^2/r^2$. Substitution of Eqs. (4) and (5) into Eq. (6) and introducing the incompressibility condition leads to the expression

$$\varphi_k = \frac{1}{2} 4\pi R^3 \dot{R}^2 \rho_l \left(\frac{\lambda \varepsilon (1 - \cos \theta_c)}{2R} + \frac{1 - \cos \theta_c}{2} \frac{R}{R + \varepsilon} + \frac{1 + \cos \theta_c}{2} \right), \quad (7)$$

where $\lambda = \rho_{sl}/\rho_l$ is the ratio of the density of the attached solid-liquid agglomerate to the density of liquid (free slurry) surrounding the loaded bubble ($\lambda > 1$ in all cases). The maximum value of φ_k is at the equilibrium state when $R = R_0$ and $\dot{R} = i\omega_p R_0 e^{i\omega_p t}$, i.e.,

$$\varphi_{k,\max} = \frac{1}{2} 4\pi R_0^3 \dot{R}^2 \rho_l \left(\frac{\lambda \varepsilon (1 - \cos \theta_c)}{2R_0} + \frac{1 - \cos \theta_c}{2} \frac{R_0}{R_0 + \varepsilon} + \frac{1 + \cos \theta_c}{2} \right) R_0^2 \omega_p^2. \quad (8)$$

The maximum potential energy associated with gas inside the bubble (as derived in Leighton (1994)) is

$$\varphi_{p,\max} = 6\pi \kappa P_0 R_0^2 \dot{R}_0^2. \quad (9)$$

Based on the law of conservation of energy, equating $\varphi_{k,\max}$ to $\varphi_{p,\max}$ gives the resonance frequency of a solids loaded bubble as

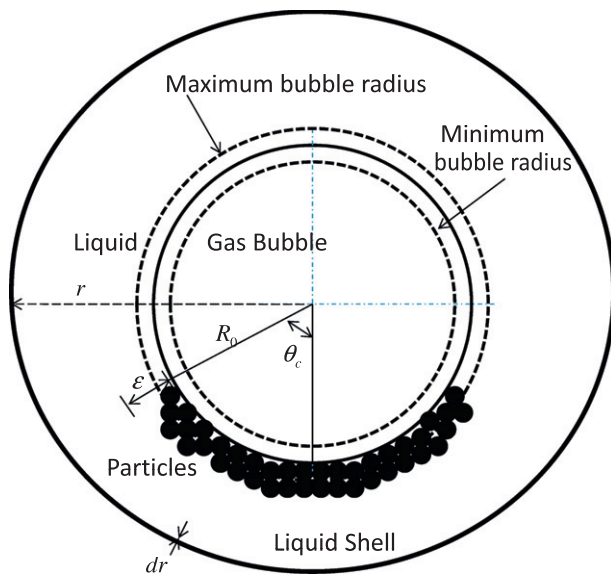


Fig. 1. Schematic view of solid particles attached to a gas bubble in liquid. θ_c is the solids coverage angle and ε is the thickness of the attached solid-liquid agglomerate layer.

$$f_p = f_0 \left(\frac{1}{\frac{\lambda \varepsilon (1 - \cos \theta_c)}{2R_0} + \frac{1 - \cos \theta_c}{2} \frac{R_0}{R_0 + \varepsilon} + \frac{1 + \cos \theta_c}{2}} \right)^{1/2}. \quad (10)$$

Eq. (10) shows that the resonance frequency of a solids-loaded bubble is determined by the bubble equilibrium radius, the corresponding unloaded bubble resonance frequency, the solids coverage angle and the thickness of the attached solid–liquid agglomerate layer. As shown in Eq. (4), the attached layer thickness is also related to the solids mass loading, bubble equilibrium radius, solids coverage angle, solids density and volumetric fraction of particles in the attached solid–liquid agglomerate.

2.2. Flotation application

In flotation, there are usually two cases of attachment, i.e., a monolayer or a multilayer of particles attached to the bubble (Omota et al., 2006a,b). The application of the model to these two cases is illustrated in the following.

2.2.1. Monolayer attachment

When the cohesive forces between particles are small and the adhesive forces between particles and the bubble are large, the particles attach to the bubble as a monolayer (Omota et al., 2006a,b). In this case, the attached solid–liquid agglomerate layer thickness $\varepsilon \ll R_0$, as the bubble size is usually much larger than the particle size in flotation. Two formulae are derived in the following: one for low density particle loading and the other for high density particle loading.

2.2.1.1. Formula 1: (low density particle loading). From the Taylor series expansion of Eq. (10) around the point of $\frac{\varepsilon}{R_0} = 0$, the following relation can be derived

$$\left(\frac{f_{p:mon}}{f_0} \right)^2 \approx 1 - \frac{1}{2} (1 - \cos \theta_c) (\lambda - 1) \frac{\varepsilon}{R_0}. \quad (11)$$

Introducing Eqs. (4) into (11), leads to the following model for estimating the monolayer solids mass loading

$$M_s \approx \frac{4\pi R_0^3 \rho_s \delta_s \left(1 - \left(\frac{f_{p:mon}}{f_0} \right)^2 \right)}{(\lambda - 1)}. \quad (12)$$

Note that the high order terms are negligible only when $\lambda < \frac{2}{1 - \cos \theta_c} + 1$. For example, for half-covered or fully covered bubbles, λ should be less than 3 or 2, respectively. This implies the model (12) can only provide accurate solutions for low density particle loading, such as coal and light metals.

2.2.1.2. Formula 2: (high density particle loading). By expanding the term $\frac{1}{1 + \varepsilon/R_0}$ in the denominator into the Taylor series and neglecting the high order terms of (ε/R_0) , Eq. (10) leads to

$$\left(\frac{f_{p:mon}}{f_0} \right)^2 \approx \frac{1}{1 + \frac{M_s(\lambda - 1)}{4\pi R_0^3 \rho_s \delta_s}}. \quad (13)$$

This approximation leads to another model for estimating the monolayer solids mass loading

$$M_s \approx \frac{4\pi R_0^3 \rho_s \delta_s \left(1 - \left(\frac{f_{p:mon}}{f_0} \right)^2 \right)}{\left(\frac{f_{p:mon}}{f_0} \right)^2 (\lambda - 1)}. \quad (14)$$

Simulation results prove that the model (14) works worse for low density particle loading estimation compared to the model (12) but provides a more flexible and accurate solution for high density particle loading, such as heavy metals. Both models lead to a direct expression for the attached solids mass, independent of

the solids coverage angle, as a function of the ratio of loaded to unloaded resonance frequency, bubble equilibrium radius, solids density and volumetric fraction, and the ratio of attached slurry to liquid density.

2.2.2. Multilayer attachment

For high particle surface hydrophobicity, the cohesive forces between particles exceed a certain limit and multilayer attachment occurs (Omota et al., 2006a). The average thickness of multilayer attachment to a bubble is typically several times the particle size; and the coverage angle decreases as layer thickness increases (Omota et al., 2006b). A special case is when the cohesive forces are higher than the adhesive forces, and then the particle–liquid agglomerate clusters and can attach to the bubble through only a few particles. In this case, a solids coverage angle of $\theta_c \approx 0$ means that Eq. (10) (with substitution of Eq. (4) to remove the now undefined ε solids layer thickness) reduces to

$$\left(\frac{f_{p:clu}}{f_0} \right)^2 \approx \frac{1}{\frac{\lambda M_s}{4\pi R_0^3 \rho_s \delta_s} + 1}, \quad (15)$$

from which, the attached solids mass loading can be estimated as

$$M_s \approx \frac{4\pi R_0^3 \rho_s \delta_s \left(1 - \left(\frac{f_{p:clu}}{f_0} \right)^2 \right)}{\left(\frac{f_{p:clu}}{f_0} \right)^2 \lambda}. \quad (16)$$

3. Experimental method

3.1. Material

The solid clear borosilicate glass microspheres (GL-0179) were purchased from MO-SCI cooperation. The microsphere surfaces have been fully acid washed and silane coated in order to render them hydrophobic, with the contact angle about 90°. The particles are within a nominal size range of $115 \pm 10 \mu\text{m}$ and the estimated median size of the particles observed herein is $115 \mu\text{m}$. The density of the glass is 2200 kg/m^3 .

3.2. Experimental rig

The experiments are performed in quiescent liquid water within a laboratory glass tank of $60 \times 60 \times 60 \text{ cm}^3$ volumetric capacity (Fig. 2). Two different sizes of air bubbles are generated, as per the protocol in Table 1 (unloaded resonance is acoustically measured), at the end of a stainless steel capillary. The delivery of air is from a Hamilton 250 μl syringe under precise control by a syringe pump (Longer Pump, Baoding, China). The capillary is bent in an L-shape so that the tip of the capillary is horizontally orientated. A particle dropping technique (Nguyen and Schulze, 2004; Verrelli et al., 2011; Wang et al., 2003) is adopted in the present work to load

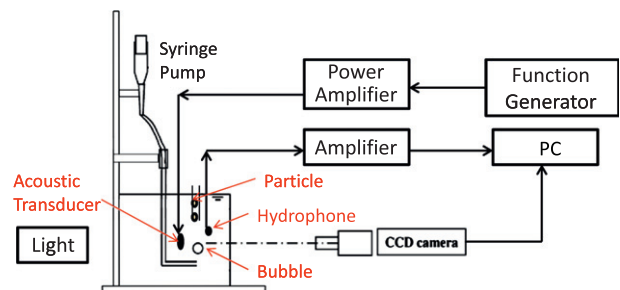


Fig. 2. Schematic of equipment setup for active acoustic measurements of particle-laden bubble oscillations.

Table 1
Capillaries and bubble size protocol.

Capillary			Bubble	
Gauge	Inner diameter (mm)	Outer diameter (mm)	Radius (mm)	Unloaded resonance (Hz)
26	0.25	0.46	0.55	5500
19	0.69	1.07	0.89	3400

the treated glass microspheres onto the stationary bubble. The current experiment setup emulates a feature in a real flotation system, i.e., particles loading begins from the underside of the bubble.

3.3. Procedure

The solids attached bubble is induced to release from the needle orifice and then driven to small amplitude pulsation (linear response) by the application of an external sound field. The advantage of this active acoustic monitoring method over a passive approach is that it produces a larger acoustic response that is more readily detectable, which is especially important for small bubbles. In this technique, the acoustic stimulus, which usually has a component oscillating at the bubble natural frequency, is sent from a transducer. The bubble responds to the stimulus by resonating at its natural frequency, with the response observed as an increase in the spectral power of the total received sound at this specific frequency.

The acoustic transducers used in these experiments are a low frequency transducer (frequency response flat to within ± 5 dB over 2–10 kHz) to generate the external stimulus for bubble oscillation and a Bruel and Kjaer hydrophone to receive the bubble response. The transducer and the needle tip are at a depth of 13 cm under the water surface and the distance between them is 5 cm. The hydrophone is placed 3 cm from the needle tip and is at a depth of 12 cm under water surface (detecting near-field acoustic emissions). The acoustic signal used to drive the bubble into low-amplitude forced oscillation is a broadband linear sweep signal, whose frequency is incremented in 25 Hz steps from 2.8 to 3.8 kHz for a bubble of 0.89 mm radius and from 5 to 6 kHz for a bubble of 0.53 mm radius, with a duty cycle of 0.4 s.

Images of the forced oscillation of the solids loaded bubble are recorded using a MotionPro X3 high speed video camera equipped with a Navitar Zoom 12 \times lens operating at 1000 frames per second. The video images are subsequently processed using Image-Pro Plus 7.0 software to determine the solids coverage geometry on the bubble surface and to analyse the dynamics of the solids attached bubble oscillation.

4. Results

4.1. Typical acoustic response

Fig. 3 shows the pressure envelope of the acoustic stimulus and the received acoustic response of a bubble (generated by the 19-gauge capillary) versus time over the same time period while the stimulus frequency is incremented in 25 Hz steps from 2.8 kHz to 3.8 kHz. The video sequences given in [Supplementary material](#) demonstrate that after detachment from the needle, a solids attached bubble in a small amplitude acoustic pressure field tends to maintain the spherical shape, regardless of the geometrical configuration of attached solids loading. The bubble dynamics is in the region of linear spherical pulsations. This result implies that non-uniform solids coverage still leads to ‘breathing’ mode bubble oscillations, supporting a key assumption in our models.

Comparison of the acoustic stimulus (the amplitude changes with time as the transducer has ± 5 dB variation over the sweep

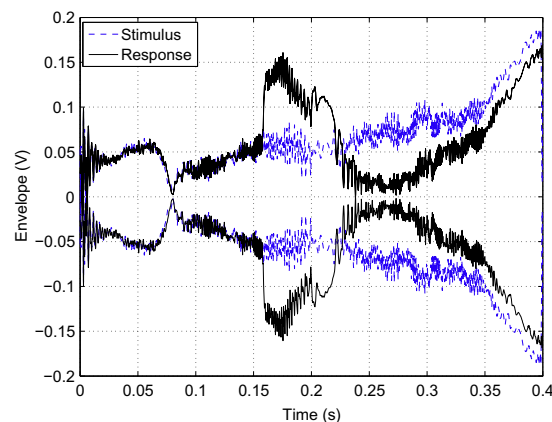


Fig. 3. Envelope of the sweep acoustic stimulus and typical acoustic response for a particle-laden bubble going through resonance.

frequency range) and the received response in Fig. 4 further reveals the following.

- I. When the loaded bubble is far from natural resonance, it tends to linear, low-amplitude forced oscillation.
- II. When the bubble is driven through natural resonance by sweep excitation, an enlarged acoustic response is initially present (as shown in Fig. 3 at around 0.16 s) followed by a sharp decrease.

These results prove that the active acoustic technique could be used to detect the natural resonance frequency of a solids attached bubble, and may actually be sensitive to the solids mass loading.

The power spectral density (PSD) of the received acoustic signal in comparison with that of the acoustic stimulus is shown in Fig. 4. The stimulus has a flat response over its swept frequency range

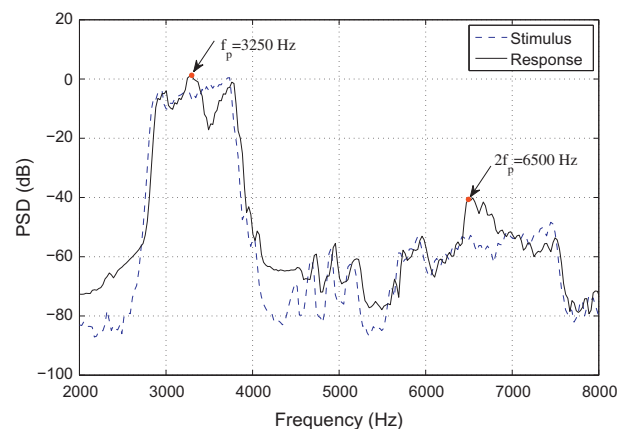


Fig. 4. PSD of the acoustic stimulus and the received acoustic response. The stimulus has a flat response over its swept frequency range from 2.8 kHz to 3.8 kHz. The increase in the power spectrum at the resonance frequency $f_p = 3250$ Hz and the second harmonic $2f_p = 6500$ Hz can be observed.

from 2.8 kHz to 3.8 kHz; while the received signal has a rise in the spectral power just before and at the resonance frequency $f_p = 3250$ Hz followed by a sharp dip. This is the characteristic through-resonance behaviour of a bubble (Leighton et al., 1996), i.e., at frequencies just less than resonance the bubble oscillation and the driving sound field are in phase, resulting in an increase in the spectral power; but at frequencies just above resonance the bubble oscillation undergoes a π phase shift such that the bubble pulsates in anti-phase with the driving sound field, resulting in the sharp dip in the power spectrum. In addition, as the bubble oscillations at resonance become large, the inherent nonlinearities in bubble acoustic response become prominent. For example, a second harmonic is generated at around 6500 Hz ($2f_p$). This piece of information could be used to more accurately estimate the fundamental resonance frequency.

4.2. Solids mass loading estimation

In this section, the measurement and analysis methodology described above is applied to estimate the solids mass loading on example bubbles and to validate the theoretical formulae developed in Section 2. Two cases featured in flotation systems are investigated: monolayer and multilayer attachment.

4.2.1. Monolayer attachment

Fig. 5 shows images of two bubbles (equilibrium radii 0.89 mm) partially covered with hydrophobic glass spheres. The solids coverage on these two example bubbles are modelled as monolayer, corresponding to strong adhesive forces between particles and bubbles, and weak cohesive forces between particles. The solids coverage angles are $\theta_c \approx 90^\circ$ in Fig. 5a and $\theta_c \approx 48^\circ$ in Fig. 5b, respectively. The particle distribution at the bubble surface shows a high packing density of solids (solids volumetric packing fraction $\delta_s \approx 0.60$ (Omota et al., 2006a) and the ratio of attached slurry to liquid density $\lambda = 1.72$).

The resonance frequencies of these two loaded bubble systems are readily measured from acoustic responses, being $f_p \approx 3300$ Hz for 90° coverage and $f_p \approx 3375$ Hz for 48° coverage. Given that the unloaded bubble in each case resonates at $f_0 = 3400$ Hz, we can estimate the thickness of attachment and the solids mass loading based on the full model (10) and the simplified monolayer attachment model (12) for low density particles. The results are listed in Table 2. It is observed that bubble mass loading estimation using the proposed acoustic emission technique is on a per bubble basis, providing milligram scale predictions. Clearly, this is much lower than the minimum 200 g of attached solids required for detection by the conventional positive displacement method (Seaman et al., 2004).

In order to independently estimate the solids mass loading on each bubble, video images of the oscillating bubbles are processed using the Image-Pro Plus software. This includes converting the image to grayscale and high-pass filtering to reduce the background noise. The layer thicknesses and coverage angles of solids attachment on the bubbles are measured from the processed images, leading to a validation estimate (via Eq. (4)) for the solids mass loading. These bubble image analysis results are used as optical references to assess the accuracy of the mass loading predictions obtained from the acoustic measurements and associated resonance frequency mathematical models.

Fig. 6 shows the attached solids mass loading estimates versus the squared ratio of the load bubble resonance to the unloaded bubble resonance, for bubbles of two different sizes (0.89 mm and 0.32 mm radius). Estimates of attached solids mass loading from the full and monolayer acoustic models and the optical reference are here compared. The shape of the monolayer model as expected from Eq. (12) is approximately a straight line as M_s

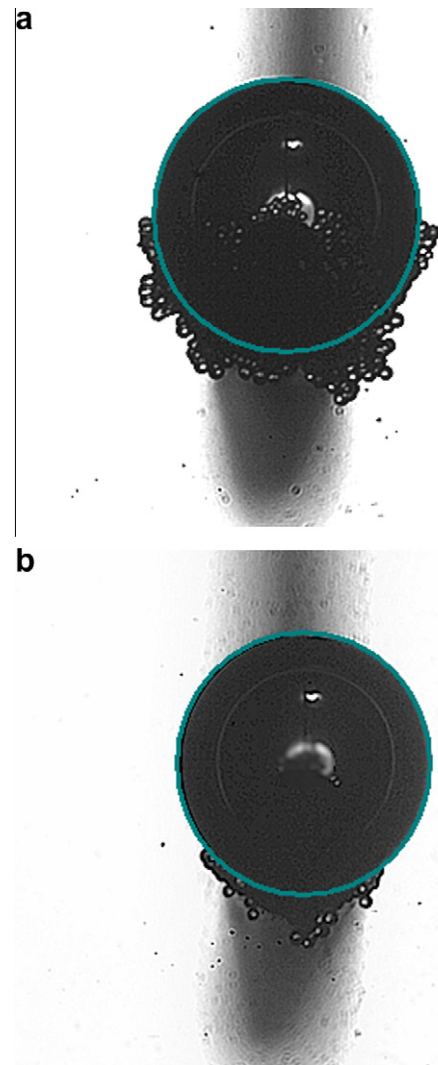


Fig. 5. Images of monolayer of hydrophobic glass spheres attached to a bubble at around (a) 90° coverage and (b) 48° coverage.

monotonically decreases with $(f_p/f_0)^2$. The mean differences between the full acoustic model and optical reference estimates are $\sim 13\%$ and $\sim 23\%$; while the simplified model tends to give comparable predictions with relative differences of $\sim 11\%$ and $\sim 20\%$, for these two sizes of bubbles. Note that Fig. 5 actually shows that solids loading on bubble surface are not a uniform monolayer distribution; there are several spots where two to three layers of particles adhere to the bubble. However, as long as the thickness of attachment is considerably lower than the bubble radius ($R_0 \gg \epsilon$), the simplified monolayer attachment model (12) should be applicable for accurate predictions. It should also be remembered that there is inherent error in the image processing method of mass loading estimation.

4.2.2. Multilayer attachment

Fig. 7 shows images of two bubbles partially covered with multiple layers of hydrophobic glass spheres. These examples of bubble loading correspond to weak adhesive forces between particles and bubbles, and strong cohesive forces between particles. Two common cases of multilayer attachment are shown, one is with a large coverage angle but only a few layers of attachment (Fig. 7a) and the other is with a small coverage angle but substantially more 'layers' of attachment (approximating cluster attachment as shown in Fig. 7b). Note that the multilayer attachment usually has what

Table 2
Experiment results of solids mass loading on a gas bubble.

Attachment	Thickness of attachment (mm)	Coverage angle θ_c (°)	Measured resonance (Hz)	Loading estimated from full model (mg)	Loading estimated from simplified model (mg)	Loading observed from images (mg)
Monolayer ($\delta_s = 0.60$)	0.13	90	3300	0.84	0.94	0.85
	0.12	48	3375	0.21	0.24	0.26
Multilayer ($\delta_s = 0.52$)	0.30	65	3250	1.12	–	1.13
	0.75	20	3350	0.28	0.19	0.26

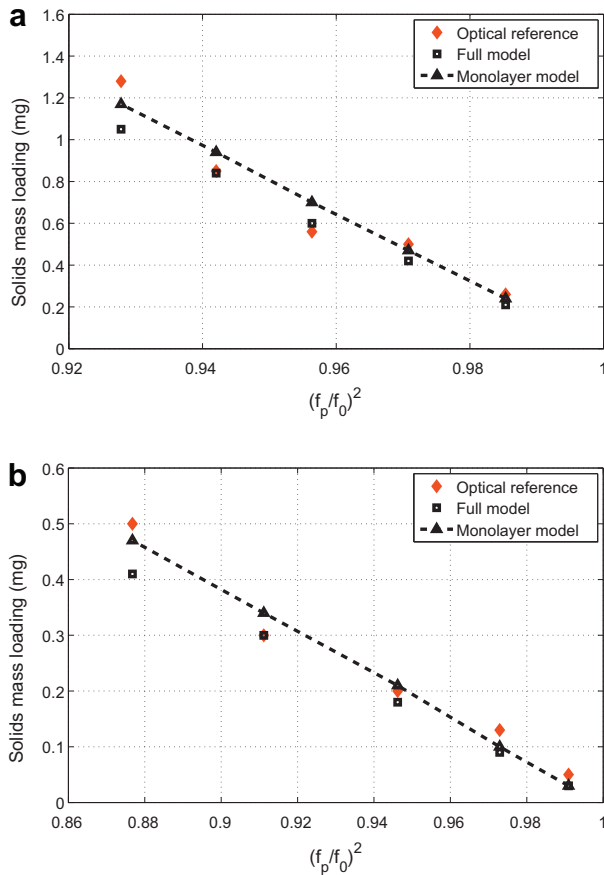


Fig. 6. Estimates of monolayer attached solids loading versus the squared ratio of the loaded bubble resonance to the unloaded bubble resonance. (a) Bubble of radius 0.89 mm and (b) bubble of radius 0.53 mm.

could be termed a medium packing capacity (solids volumetric packing fraction $\delta_s = 0.52$ (Omota et al., 2006a)), leading to a ratio of $\lambda \sim 1.6$ of attached slurry to liquid density.

The resonance frequencies of these two loaded bubble systems are $f_p \approx 3250$ Hz for 65° coverage and $f_p \approx 3350$ Hz for 20° coverage. The unloaded bubbles again resonate at $f_0 = 3400$ Hz and Table 2 shows the acoustic and optical estimates of the solids mass loadings. Fig. 7a shows that in this large coverage angle case, there is a relatively substantial thickness of solids attachment, perhaps half of the bubble radius. In this case the full acoustic model gives an accurate match ($\sim 6\%$ relative difference) compared to the reference value. The thin layer acoustic model is not appropriate in this case.

For the approximate cluster attachment case, Fig. 8 demonstrates that both the full model (Eq. (10)) and the simplified cluster model (Eq. (16)) acoustic estimates of attached solids mass loading agree reasonably well with the optical reference estimates. Two different sizes of bubbles with a variety of solids mass loading

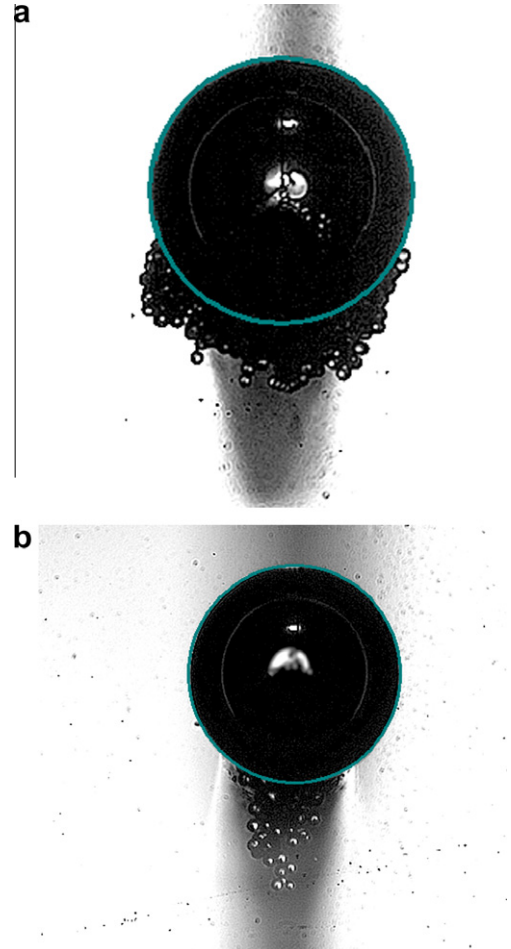


Fig. 7. Images of multilayer of hydrophobic glass spheres attached to a bubble at around (a) 65° coverage and (b) 20° coverage.

are investigated. Again, estimates from the cluster model monotonically decrease with the squared ratio of the loaded to unloaded resonance as suggested from Eq. (16). The relative differences between the full model and optical reference estimates are both $\sim 9\%$; while for the simplified cluster model the relative differences are $\sim 24\%$ and $\sim 20\%$ for these two sizes of bubbles, respectively. The relative larger prediction errors from the simplified cluster model may be due to the fact that in the approximate cluster attachment experiments, solids still attach to the bubble surface with a coverage angle between 10° and 20°.

5. Discussion

The experimental results detailed above support the view that the loaded bubble resonance frequency changes strongly with

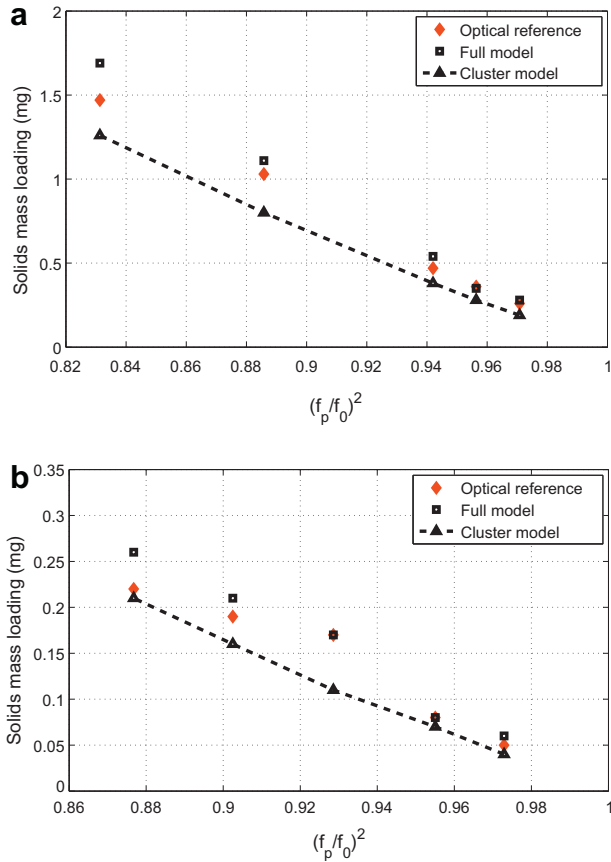


Fig. 8. Estimates of cluster attached solids loading versus the squared ratio of the loaded bubble resonance to the unloaded bubble resonance. (a) Bubble of radius 0.89 mm and (b) bubble of radius 0.32 mm.

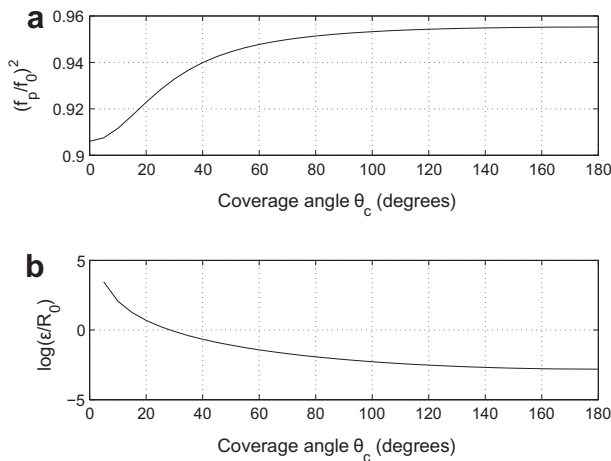


Fig. 9. Plot of (a) the squared ratio of the load bubble resonance to the unloaded bubble resonance and (b) the thickness of the attached solid-liquid agglomerate layer as a function of the coverage angle. The bubble radius is 1 mm; the attached solids mass is 1 mg.

two geometrical covering parameters, the coverage angle and the thickness of attachment. In order to demonstrate the theoretical dependence of resonance frequency on solids coverage angle, simulations of acoustic response (based on Eq. (10) for the full model) are performed with a fixed amount of mass (1 mg, density 2200 kg/m³) loaded on a bubble of given size (radius of 1 mm), with the

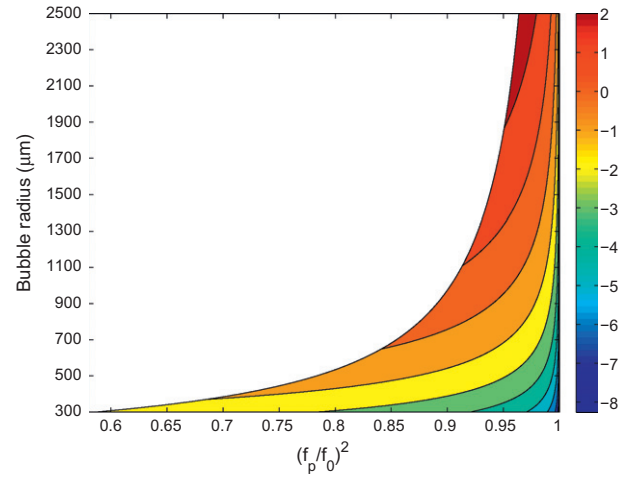


Fig. 10. Plot of log solids loading (mg) monolayer attached on bubble with the bubble radius (μm) and the squared ratio of the loaded bubble resonance to the unloaded bubble resonance.

coverage angle changing through 0–180°. Fig. 9a shows that the lowest resonance frequency is associated with cluster attachment ($\theta_c = 0^\circ$). Clearly, the more uniform the covering on the bubble surface, the higher the resonance frequency. The prediction of the full model (Eq. (10)) smoothly tends to the prediction of the zero coverage angle model (Eq. (16)). Comparison of Fig. 9a and b also demonstrates that when the thickness of the attached solid-liquid agglomerate layer is much less than the bubble radius ($\theta_c \geq 80^\circ$), the resonance frequency has a negligible dependence on the coverage angle as expected from the monolayer attachment models (Eqs. (12) and (14)). This finding is important because it supports the view that in many important cases, changes in bubble acoustic fundamental resonance frequency with the addition of solids can be reliably interpreted in terms of the attached solids mass loading and bubble equilibrium size alone.

The range of squared ratio of solids loaded to unloaded bubble resonance frequency in Fig. 9 corresponds to resonance frequencies $f_p \approx 2.87\text{--}2.95$ kHz. These variations in resonance frequency should be readily detectable with a suitable acoustic emission monitoring system hence the proposed method could be used to distinguish differences in both bubble solids mass loading and in some cases coverage geometry provided the equilibrium bubble size is independently known.

In a flotation cell, the packing of particles on a bubble is generally assumed to be mono-layered (Bournival and Ata, 2010). Fig. 10 is a filled contour plot of bubble solids loading (monolayer attachment based on Eq. (12)) as a function of the squared ratio of solids loaded to unloaded resonance frequencies and equilibrium bubble radius. This plot demonstrates a straightforward application of the proposed model for the on-line monitoring of attached solids on a pulp bubble. In this simulation, the bubble radius varies from 0.3 mm to 2.5 mm. The packing of the glass microspheres (radius $R_p = 60 \mu\text{m}$, density ρ_s of 2200 kg/m³) on the bubble is assumed to be with a high density ($\delta_s = 0.6$) and maximum solids coverage angle of 180°. In flotation, it is generally accepted that the surface of pulp bubbles are half-covered at maximum. However, fully covered bubbles have also been reported in laboratory conditions (Bournival and Ata, 2010; Uribe-Salas et al., 2003). The maximum mass that can be loaded on the bubble is obtained by (Omota et al., 2006a)

$$M_s = 8\pi R_p^3 \rho_s \delta_s \left(1 + \frac{R_0}{R_p}\right)^2, \quad (17)$$

where R_0 and R_p are the radius of bubble and particle, respectively. The squared ratio of the solids loaded to unloaded bubble resonance frequencies can be obtained from acoustic measurements. The bubble radius could be independently estimated by image analysis. For example, given $R_0 = 890 \mu\text{m}$, our theoretical estimate for the squared ratio of solids loaded to unloaded bubble acoustic resonance frequency (based on the monolayer solids attachment model) is $(f_p/f_0)^2 = 0.942$, leading to an estimate of ~ 0.94 mg for the attached solids mass loading. This estimate is exactly the result of the first monolayer attachment experiment, which is highly encouraging. The plot further shows that with the same amount of mass attached, the smaller the bubble, the lower the squared ratio of loaded to unloaded resonance frequencies. This means the decrease in resonance frequency with solids loading is significantly larger with smaller bubbles. Therefore, the proposed acoustic emission monitoring technique is especially applicable to flotation applications, as bubbles in a flotation cell are usually less than 1 mm in equilibrium radius.

6. Conclusion

An acoustic emission technique to estimate bubble attached solids mass loading has been described in this paper. The method is based on the fact that the coating of solids on a bubble surface increases the acoustic radiative mass of the system and thus results in a decrease in the fundamental resonance frequency. An analytical model was derived to express the resonance frequency of a loaded bubble as a function of the unloaded bubble resonance frequency, the bubble equilibrium radius, the solids coverage angle and the attached solids mass loading. Experiments based on an active acoustic monitoring technique were performed to stimulate single loaded bubbles into low-amplitude resonant oscillation, allowing the fundamental resonance frequency to be measured. Predictions of bubble solids mass loading were derived from a number of theoretical acoustic fundamental resonance models formulated under various approximations for layer thickness and coverage angle. These models are suitable for linear bubble oscillations at low-amplitude acoustic forcing conditions. Validation of the theoretical bubble resonance models was achieved by comparison of the predicted attached solids mass loadings with estimates obtained from optical observations. Experimental results show that the developed acoustic technique can measure solids mass loading for single bubbles to ~ 0.1 mg accuracy. A variety of monolayer or multilayer theoretical resonance models may be applied to analysis of the acoustic emissions, depending on the coverage geometry of solids on the bubbles in the system. In addition, simulation results show that the developed methodology is especially applicable to systems with small bubbles, such as flotation systems. A key consideration in the application of the method to flotation systems is the ability to insonate and to detect acoustic emissions from only a small number of bubbles and hence avoid group acoustic effects.

Clearly, the proposed bubble acoustic monitoring system requires an independent measurement for bubble equilibrium size in order to unambiguously estimate solids loading. Besides the fundamental resonance, a second harmonic becomes prominent in experiments when the loaded bubble is induced into non-linear oscillation by stronger acoustic forcing. In addition, the quality

factor (or the Q factor) could be used to relate the bubble mass loading to the oscillation damping characteristics. Further work is being performed to explore this information for potential simultaneous on-line acoustic monitoring of both bubble size and attached solids in industrial flotation cells.

Acknowledgements

We would like to thank Dr. Bart Follink and Dr. Marcus Zipper for their support and advice to this work. We also thank Dr. David Verrelli for helpful discussions on high-speed photographic recordings. Finally, we acknowledge Mr. Mike Millen and Dr. Yi Liu for their constructive comments and suggestions that helped to improve the presentation of this paper.

Appendix A. Supplementary material

Supplementary data associated with this article can be found, in the online version, at [doi:10.1016/j.mineng.2012.02.007](https://doi.org/10.1016/j.mineng.2012.02.007).

References

- Barbian, N., Cilliers, J.J., Morar, S.H., Bradshaw, D.J., 2007. Froth imaging, air recovery and bubble loading to describe flotation bank performance. *International Journal of Mineral Processing* 84 (1–4), 81–88.
- Bhondyay, C., 2010. Measurements of particle loading on bubbles in froth flotation. In: Faculty of Engineering and the Built Environment. University of the Witwatersrand.
- Bournival, G., Ata, S., 2010. Packing of particles on the surface of bubbles. *Minerals Engineering* 23, 111–116.
- Bradshaw, D.J., O'Connor, C.T., 1996. Measurement of the sub-process of bubble loading in flotation. *Minerals Engineering* 9 (4), 443–448.
- Dyer, C., 1995. An Investigation into the Properties of the Froth Phase in Flotation Process. University of the Witwatersrand.
- Leighton, T.G., 1994. *The Acoustic Bubble*. Academic Press, New York.
- Leighton, T.G., Phelps, A.D., Ramble, D.G., Sharpe, D.A., 1996. Comparison of the abilities of eight acoustic techniques to detect and size a single bubble. *Ultrasonics* 34 (6), 661–667.
- Minnaert, M., 1993. On musical air bubbles and the sounds of running water. *Philosophical Magazine* 16 (104), 235–248.
- Moys, M.H., Yianatos, J., Larenas, J., 2010. Measurement of particle loading on bubbles in the flotation process. *Minerals Engineering* 23 (2), 131–136.
- Nguyen, A.V., Schulze, H.J., 2004. *Colloidal Science of Flotation*. Marcel Dekker Inc., New York.
- Omota, F., Dimian, A.C., Bliet, A., 2006a. Adhesion of solid particles to gas bubbles. Part 1: Modelling. *Chemical Engineering Science* 61 (2), 823–834.
- Omota, F., Dimian, A.C., Bliet, A., 2006b. Adhesion of solid particles to gas bubbles. Part 2: Experimental. *Chemical Engineering Science* 61 (2), 835–844.
- Ross, V.E., 1997. Particle-bubble attachment in flotation froths. *Minerals Engineering* 10 (7), 695–706.
- Sadr-Kazemi, N., Cilliers, J.J., 2000. A technique for measuring flotation bubble shell thickness and concentration. *Minerals Engineering* 13 (7), 773–776.
- Seaman, D.R., Franzidis, J.P., Manlapig, E.V., 2004. Bubble load measurement in the pulp zone of industrial flotation machines – a new device for determining the froth recovery of attached particles. *International Journal of Mineral Processing* 74 (1–4), 1–13.
- Uribe-Salas, A., de Lira-Gomez, P., Perez-Garibay, R., Nava-Alonso, F., Magallanes-Hernandez, L., Lara-Valenzuela, C., 2003. Overloading of gas bubbles in column flotation of coarse particles and effect upon recovery. *International Journal of Mineral Processing* 71 (1–4), 167–178.
- Ventura-Medina, E., Barbian, N., Cilliers, J.J., 2004. Solids loading and grade on mineral froth bubble lamellae. *International Journal of Mineral Processing* 74 (1–4), 189–200.
- Verrelli, D.I., Koh, P.T.L., Nguyen, A.V., 2011. Particle–bubble interaction and attachment in flotation. *Chemical Engineering Science* 66 (23), 5910–5921.
- Wang, W.X., Zhou, Z.A., Nandakumar, K., Xu, Z.H., Masliyah, J.H., 2003. Attachment of individual particles to a stationary air bubble in model systems. *International Journal of Mineral Processing* 68 (1–4), 47–69.